

Supporting Information for:

Supramolecular approach for fine-tuning of the bright luminescence from zero-dimensional antimony(III) halides

Viktoriia Morad,^{†‡} Sergii Yakunin,^{†‡} and Maksym V. Kovalenko^{†,‡,*}

[†]Laboratory of Inorganic Chemistry, Department of Chemistry and Applied Bioscience, ETH Zürich, Vladimir Prelog Weg 1, CH-8093 Zürich, Switzerland

[‡]Laboratory for Thin Films and Photovoltaics, Empa – Swiss Federal Laboratories for Materials Science and Technology, Überlandstrasse 129, CH-8600 Dübendorf, Switzerland

1. Materials

Potassium bromide (KBr, Ph. Eur., Fluka, 1kg), rubidium bromide (RbBr, metal basis, 99.8%, ABCR, 25g), cesium bromide (CsBr, trace metal basis, 99.9%, Aldrich, 100g), cesium chloride, rubidium chloride, barium bromide anhydrous (BaBr₂, 99.999%, ABCR, 5g), barium chloride anhydrous (BaCl₂, 99.995%, metals basis, ABCR, 5g), antimony(III) bromide (SbBr₃, 99%, ABCR, 50g), antimony (III) chloride (SbCl₃, 99.9%, ABCR, 25g), 1,4,7,10,13,16-Hexaoxacyclooctadecane (18-crown-6, 99%, Apollo Scientific Ltd, 100g), N,N-dimethylformamide (DMF, 99.8%, Extra Dry over Molecular Sieve, AcroSeal®). Alkali halides were additionally dried under at 50 °C and 10⁻⁴ mbar for 12 h. All chemicals were stored in the air-free Ar-filled glovebox with H₂O and O₂ levels <0.01 ppm. Organic solvents were used as received without further purification.

2. Synthesis

In general, hybrid phosphors were obtained from SbX₃, 18-crown-6 and metal halide (CsX, RbX, KX, BaX₂) precursor solutions in dimethylformamide (DMF) or acetonitrile (ACN). Typical precursor solutions were prepared by mixing 0.25 mmol SbX₃ and stoichiometric amounts of 18-crown-6 and metal halide in 10 ml (for bromides) or 20 ml (for chlorides) of corresponding organic solvent by stirring on a hot plate at about 80°C until all solids were dissolved. The powders were precipitated either by slow cooling or by injecting precursor solutions into excess of diethyl ether. After separation by suction or centrifugation, powdered precipitates were additionally washed with acetone. For single crystal growth, the same as described above precursor solution was placed into an antisolvent slow diffusion chamber with diethyl ether.

[C@A][C@Ba][SbBr₆] (A = Cs, Rb). SbBr₃ (0.25 mmol), ABr (0.25 mmol), BaBr₂·2H₂O and 18-crown-6 (0.5 mmol) were dissolved in DMF (10 ml) upon stirring and heating. Powdered product was obtained by injecting precursor solution into two-fold excess of diethyl ether. For growth of single crystals, 1 ml of precursor solution was filtered and set up with 2 ml of diethyl ether in an antisolvent slow diffusion chamber.

[C@Ba]₄[SbX₆]₂[Sb₂X₈] (X = Cl, Br). SbX₃ (0.25 mmol), BaX₂·2H₂O (0.25 mmol) and 18-crown-6 (0.25 mmol) were dissolved in DMF (10 ml for Br, 20 ml for Cl) upon stirring and heating to 80°C. Microcrystalline product was obtained by slowly cooling to room temperature. For growth

of single crystals, 1 ml of precursor solution was filtered and set up with 2 ml of diethyl ether in an antisolvent slow diffusion chamber.

[C@A]₂SbX₅ (A = Cs, Rb, K, X = Cl, Br). SbX₃ (0.25 mmol), AX (0.5 mmol) and 18-crown-6 (0.5 mmol) were dissolved in DMF (10 ml for Br, 20 ml for Cl) upon stirring and heating. For [C@Cs]₂SbBr₅, slow diffusion of diethyl ether into DMF precursor solution was employed to obtain the product, as rapid injection into diethyl ether resulted in formation of [C@Cs]₂CsSbBr₆. For other [C@A]₂SbX₅ compounds, rapid injection into excess of diethyl ether resulted in the formation of the target product. For growth of single crystals, 1 ml of precursor solution was filtered and set up with 2 ml of diethyl ether in an antisolvent slow diffusion chamber.

[C@Cs]₂CsSbBr₆. SbBr₃ (0.25 mmol), CsBr (0.75 mmol) and 18-crown-6 were (0.5 mmol) dissolved in 10 ml DMF upon heating and stirring. The powdered product was obtained by injecting the precursor solution into excess of diethyl ether. For growth of single crystals, 1 ml of precursor solution was filtered and set up with 2 ml of diethyl ether in an antisolvent slow diffusion chamber.

3. Characterization

Powder X-ray diffraction (XRD) patterns were collected in transmission (Debye-Scherrer-Geometry) with STADI P diffractometer (STOE& Cie GmbH), equipped with a silicon strip MYTHEN 1K Detector (Fa. DECTRIS) with a curved Ge (111)-Monochromator (CuK α 1=1.54056Å). For the measurement, a grounded powder was placed between the adhesive tape.

Single-crystal XRD measurements were conducted on Oxford Xcalibur S diffractometer equipped with Sapphire 3 CCD detector and molybdenum (MoK α =0.71073 Å) sealed tube as an X-ray source. Crystals were tip-mounted on a micromount with paraffin oil. The data were processed with Oxford Diffraction CrysAlis Pro software, structure solution and refinement was performed with SHELXS and SHELXL respectively, imbedded in the Olex2 package.¹⁻² The crystal structure of the synthesized compound was solved with direct methods, light elements (C, N) were located in the difference Fourier map, most of the positions of the cations were refined as rigid groups, and hydrogen atoms were placed at calculated positions.

Photoluminescence (PL) emission and excitation steady-state spectra were recorded either with FluoroMax4-Plus-P (Horiba Jobin Yvon) equipped with 150W Xe lamp. The samples were prepared as powders encapsulated in 10x10 mm quartz slides.

Absolute quantum yields were measured using a Quantaaurus-QY spectrometer from Hamamatsu in a powder mode. The powder samples were encapsulated in the quartz slides prior to the measurement.

PL relaxation traces were recorded with a FluoTime 300 spectrometer from PicoQuant GmbH equipped with a TimeHarp 260 PICO counting unit and, for variation of sample temperature, coupled with a CS204, closed-cycle helium cryostat, from Advanced Research Systems. As an excitation source for time-resolved PL traces, a frequency tripled Nd:YAG laser (wavelength of 355 nm, the power density of about 10 mW cm⁻², pulse duration 10 ps). A scattering light from excitation was suppressed on the entrance of emission monochromator by 400 nm longpass filter. The samples were prepared as powders encapsulated in 10x10 mm quartz slides.

UV-Vis absorbance spectra of the microcrystalline powders were collected using a Jasco V670 spectrophotometer equipped with deuterium (D2) lamp (190 – 350 nm) for use in UV, a halogen lamp (330 – 2700 nm) for use in UV/NIR, and an integrating sphere (ILN-725) with a working

wavelength range of 220 – 2200 nm. The absorbance spectra were estimated from diffuse reflectance measured on the powdered crystals transformed into Kubelka-Munk function.

Raman spectroscopy was measured on microcrystalline samples using a Horiba LabRAM HR Evolution confocal microscope with a laser excitation of 785 nm operated at 300 mW. A 50x lens was used to focus on a flat surface of a micron-scale crystal, and repeated measurements confirm the reproducibility of the spectra.

Photostability tests were conducted on the powdered samples, incapsulated in 10x10 mm quartz slides, by recording PL spectra every 10 minutes under constant irradiation of the 405 nm 300 mW laser, resulting in power density of 2.5 W/cm².

4. Computational details

Calculations were carried out at the Density Functional Theory level as implemented in the open-source cp2k quantum chemistry code. A doubled crystallographic unit cells of compounds containing were used. A mixed plane-wave and Gaussian basis set approach was used to describe the wave function and electronic density, respectively. The kinetic energy cutoff of the plane-wave basis was set to 400 Rydberg, while a double- ζ basis set with polarization functions was employed to describe the molecular orbitals. Density of States (DOS), emission and excitation energies were calculated using Perdew-Burke-Ernzerhof (PBE) exchange-correlation functional. Scalar relativistic effects have been accounted for by using effective core potential functions in the basis set. Spin-orbit coupling effects were not included. Calculations with lattice relaxation for the ground state geometry optimization were performed to account for statistical disorder in the experimental crystal structures. Unit cell parameters were taken from experimental data and not relaxed, whereas atomic coordinates were optimized until the force reached 0.023 eV/Å. For the excited state geometry, the unrestricted Kohn-Sham approach with a triplet multiplicity was used, unit cell was not optimized, while atomic coordinates were optimized until the force reached 0.023 eV/Å.

For the band structure calculations, Vienna ab initio simulations package (VASP) was used. The projector augmented wave (PAW) potentials for atoms were used. For generalized gradient approximation (GGA) Perdew-Burke-Ernzerhof exchange-correlation functional (PBE) was used. Ionic minimization was performed until all forces on atoms were smaller than 0.001 eV/Å. A mixture of blocked Davidson iteration scheme and subsequent residual minimization scheme, direct inversion in the iterative subspace (RMM-DIIS) algorithm was used for the electronic optimization. Spin-orbit coupling (SOC) was not taken into account due to known self-interaction error that raises valence band maximum. Band structure was calculated along a high-symmetry k-points path according to Bradley and Cracknell.

Table S1. Crystal data and structure refinement for [C@K]₂SbBr₅.

Empirical formula	C ₃₀ H ₆₂ Br ₅ K ₂ N ₂ O ₁₄ Sb
Formula weight	1274.31
Temperature/K	100.00(10)
Crystal system	triclinic
Space group	P-1
a/Å	10.3871(8)
b/Å	10.5079(7)
c/Å	11.1570(9)
α/°	81.641(6)
β/°	81.407(7)
γ/°	83.885(6)
Volume/Å ³	1186.80(16)
Z	1
ρ _{calc} /cm ³	1.783
μ/mm ⁻¹	5.022
F(000)	632.0
Crystal size/mm ³	0.8 × 0.5 × 0.1
Radiation	MoKα (λ = 0.71073)
2Θ range for data collection/°	3.932 to 65.268
Index ranges	-14 ≤ h ≤ 15, -15 ≤ k ≤ 15, -16 ≤ l ≤ 16
Reflections collected	11717
Independent reflections	7098 [R _{int} = 0.0276, R _{sigma} = 0.0580]
Data/restraints/parameters	7098/0/253
Goodness-of-fit on F ²	1.104
Final R indexes [I >= 2σ (I)]	R ₁ = 0.0403, wR ₂ = 0.0866
Final R indexes [all data]	R ₁ = 0.0534, wR ₂ = 0.0933
Largest diff. peak/hole / e Å ⁻³	1.34/-1.43

Table S2. Crystal data and structure refinement for [C@Ba]₄[SbBr₆]₂[Sb₂Br₈].

Empirical formula	C _{31.5} H _{65.5} Ba ₂ Br ₁₀ N _{2.5} O _{14.5} Sb ₂
Formula weight	2028.64
Temperature/K	200.01(12)
Crystal system	triclinic
Space group	P-1
a/Å	8.9339(2)
b/Å	13.8500(4)
c/Å	24.0142(7)
α/°	80.825(2)
β/°	86.605(2)
γ/°	89.767(2)
Volume/Å ³	2928.18(14)
Z	2
ρ _{calc} /cm ³	2.301

μ/mm^{-1}	9.116
F(000)	1904.0
Crystal size/ mm^3	$0.146 \times 0.065 \times 0.023$
Radiation	Mo K α ($\lambda = 0.71073$)
2Θ range for data collection/ $^\circ$	3.442 to 61.016
Index ranges	$-12 \leq h \leq 12, -19 \leq k \leq 19, -34 \leq l \leq 34$
Reflections collected	61562
Independent reflections	17895 [$R_{\text{int}} = 0.0680, R_{\text{sigma}} = 0.0743$]
Data/restraints/parameters	17895/0/496
Goodness-of-fit on F^2	1.023
Final R indexes [$I \geq 2\sigma(I)$]	$R_1 = 0.0503, wR_2 = 0.0999$
Final R indexes [all data]	$R_1 = 0.0895, wR_2 = 0.1160$
Largest diff. peak/hole / $e \text{ \AA}^{-3}$	2.73/-2.48

Table S3. Crystal data and structure refinement for $[\text{C}@\text{Cs}][\text{C}@\text{Ba}][\text{SbBr}_6]$.

Empirical formula	$\text{C}_{29.35}\text{H}_{60.48}\text{BaBr}_6\text{CsN}_{1.78}\text{O}_{13.78}\text{Sb}$
Formula weight	1530.44
Temperature/K	120.01(19)
Crystal system	trigonal
Space group	R-3
$a/\text{\AA}$	14.0504(3)
$b/\text{\AA}$	14.0504(3)
$c/\text{\AA}$	21.4176(5)
$\alpha/^\circ$	90
$\beta/^\circ$	90
$\gamma/^\circ$	120
Volume/ \AA^3	3661.69(19)
Z	3
$\rho_{\text{calc}}/\text{cm}^3$	2.082
μ/mm^{-1}	7.055
F(000)	2194.0
Crystal size/ mm^3	$0.208 \times 0.18 \times 0.071$
Radiation	Mo K α ($\lambda = 0.71073$)
2Θ range for data collection/ $^\circ$	3.85 to 61.004
Index ranges	$-20 \leq h \leq 20, -20 \leq k \leq 20, -30 \leq l \leq 30$
Reflections collected	26387
Independent reflections	2495 [$R_{\text{int}} = 0.0464, R_{\text{sigma}} = 0.0226$]
Data/restraints/parameters	2495/0/82
Goodness-of-fit on F^2	1.182
Final R indexes [$I \geq 2\sigma(I)$]	$R_1 = 0.0381, wR_2 = 0.0769$
Final R indexes [all data]	$R_1 = 0.0485, wR_2 = 0.0802$
Largest diff. peak/hole / $e \text{ \AA}^{-3}$	0.88/-0.89

Table S4. Crystal data and structure refinement for $[\text{C}@\text{Rb}]_2\text{SbCl}_5$.

Empirical formula	C ₃₀ H ₆₂ Cl ₅ N ₂ O ₁₄ Rb ₂ Sb
Formula weight	1144.75
Temperature/K	229.96(14)
Crystal system	triclinic
Space group	P-1
a/Å	10.3975(5)
b/Å	10.4680(6)
c/Å	11.1155(6)
α/°	81.237(5)
β/°	80.582(4)
γ/°	82.112(4)
Volume/Å ³	1171.73(11)
Z	1
ρ _{calc} /cm ³	1.622
μ/mm ⁻¹	2.995
F(000)	578.0
Crystal size/mm ³	1 × 0.985 × 0.673
Radiation	Mo Kα (λ = 0.71073)
2θ range for data collection/°	3.964 to 65.506
Index ranges	-15 ≤ h ≤ 15, -15 ≤ k ≤ 15, -16 ≤ l ≤ 16
Reflections collected	14295
Independent reflections	7718 [R _{int} = 0.0328, R _{sigma} = 0.0595]
Data/restraints/parameters	7718/1/231
Goodness-of-fit on F ²	1.025
Final R indexes [I >= 2σ (I)]	R ₁ = 0.0417, wR ₂ = 0.0878
Final R indexes [all data]	R ₁ = 0.0639, wR ₂ = 0.0980
Largest diff. peak/hole / e Å ⁻³	0.72/-0.81

Table S5. Crystal data and structure refinement for [C@Cs]₂SbCl₅.

Empirical formula	C ₂₇ H ₅₅ Cl ₅ Cs ₂ NO ₁₃ Sb
Formula weight	1166.54
Temperature/K	230.0(2)
Crystal system	monoclinic
Space group	P2 ₁ /c
a/Å	21.1006(3)
b/Å	8.53683(13)
c/Å	24.3975(4)
α/°	90
β/°	98.4941(15)
γ/°	90
Volume/Å ³	4346.57(12)
Z	4
ρ _{calc} /cm ³	1.783
μ/mm ⁻¹	2.646
F(000)	2296.0
Crystal size/mm ³	0.12 × 0.092 × 0.01

Radiation	Mo K α ($\lambda = 0.71073$)
2 Θ range for data collection/ $^{\circ}$	3.642 to 59.15
Index ranges	-29 \leq h \leq 29, -11 \leq k \leq 11, -33 \leq l \leq 33
Reflections collected	83623
Independent reflections	12187 [$R_{\text{int}} = 0.0839$, $R_{\text{sigma}} = 0.0571$]
Data/restraints/parameters	12187/616/631
Goodness-of-fit on F ²	0.995
Final R indexes [$I \geq 2\sigma(I)$]	$R_1 = 0.0376$, $wR_2 = 0.0519$
Final R indexes [all data]	$R_1 = 0.0690$, $wR_2 = 0.0587$
Largest diff. peak/hole / e \AA^{-3}	0.49/-0.53

Table S6. Crystal data and structure refinement for [C@Rb]₂SbBr₅.

Empirical formula	C ₃₀ H ₆₂ Br ₅ N ₂ O ₁₄ Rb ₂ Sb
Formula weight	1367.05
Temperature/K	250.00(10)
Crystal system	triclinic
Space group	P-1
a/ \AA	10.5860(4)
b/ \AA	10.6601(6)
c/ \AA	11.3458(5)
$\alpha/^{\circ}$	80.574(4)
$\beta/^{\circ}$	80.343(3)
$\gamma/^{\circ}$	82.145(4)
Volume/ \AA^3	1237.29(10)
Z	1
$\rho_{\text{calc}}/\text{cm}^3$	1.835
μ/mm^{-1}	6.603
F(000)	668.0
Crystal size/ mm^3	0.4 \times 0.2 \times 0.2
Radiation	Mo K α ($\lambda = 0.71073$)
2 Θ range for data collection/ $^{\circ}$	3.68 to 58.59
Index ranges	-14 \leq h \leq 13, -14 \leq k \leq 14, -15 \leq l \leq 14
Reflections collected	19733
Independent reflections	5954 [$R_{\text{int}} = 0.0290$, $R_{\text{sigma}} = 0.0283$]
Data/restraints/parameters	5954/1/231
Goodness-of-fit on F ²	1.027
Final R indexes [$I \geq 2\sigma(I)$]	$R_1 = 0.0278$, $wR_2 = 0.0657$
Final R indexes [all data]	$R_1 = 0.0361$, $wR_2 = 0.0690$
Largest diff. peak/hole / e \AA^{-3}	0.80/-0.83

Table S7. Crystal data and structure refinement for [C@Cs]₂SbBr₅.

Empirical formula	C ₂₇ H ₅₅ Br ₅ Cs ₂ NO ₁₃ Sb
Formula weight	1388.84
Temperature/K	120.02(13)
Crystal system	monoclinic

Space group	P2 ₁
a/Å	10.1265(2)
b/Å	15.3814(2)
c/Å	14.2252(2)
α/°	90
β/°	92.2680(10)
γ/°	90
Volume/Å ³	2213.98(6)
Z	2
ρ _{calc} /cm ³	2.083
μ/mm ⁻¹	6.808
F(000)	1328.0
Crystal size/mm ³	0.8 × 0.2 × 0.05
Radiation	MoKα (λ = 0.71073)
2Θ range for data collection/°	3.902 to 65.494
Index ranges	-15 ≤ h ≤ 14, -23 ≤ k ≤ 22, -21 ≤ l ≤ 20
Reflections collected	48884
Independent reflections	14990 [R _{int} = 0.0354, R _{sigma} = 0.0401]
Data/restraints/parameters	14990/1/445
Goodness-of-fit on F ²	1.047
Final R indexes [I >= 2σ (I)]	R ₁ = 0.0416, wR ₂ = 0.0951
Final R indexes [all data]	R ₁ = 0.0467, wR ₂ = 0.0978
Largest diff. peak/hole / e Å ⁻³	1.17/-1.07
Flack parameter	0.067(10)

Table S8. Crystal data and structure refinement for [C@Cs]₂CsSbBr₆.

Empirical formula	C ₂₄ H ₄₈ Br ₆ Cs ₃ O ₁₂ Sb
Formula weight	1528.56
Temperature/K	120.01(18)
Crystal system	orthorhombic
Space group	Pna2 ₁
a/Å	31.9947(6)
b/Å	9.10191(15)
c/Å	14.9567(3)
α/°	90
β/°	90
γ/°	90
Volume/Å ³	4355.57(14)
Z	4
ρ _{calc} /cm ³	2.331
μ/mm ⁻¹	8.656
F(000)	2856.0
Crystal size/mm ³	0.919 × 0.325 × 0.195
Radiation	Mo Kα (λ = 0.71073)
2Θ range for data collection/°	4.652 to 65.526

Index ranges	-46 ≤ h ≤ 48, -13 ≤ k ≤ 13, -22 ≤ l ≤ 22
Reflections collected	92134
Independent reflections	15190 [R _{int} = 0.0610, R _{sigma} = 0.0427]
Data/restraints/parameters	15190/1/416
Goodness-of-fit on F ²	1.106
Final R indexes [I ≥ 2σ (I)]	R ₁ = 0.0423, wR ₂ = 0.0936
Final R indexes [all data]	R ₁ = 0.0486, wR ₂ = 0.0971
Largest diff. peak/hole / e Å ⁻³	0.90/-1.16
Flack parameter	0.494(14)

Table S9. Crystal data and structure refinement for [C@Rb][C@Ba][SbBr₆].

Empirical formula	C _{28.5} H _{58.5} BaBr ₆ N _{1.5} O _{13.5} RbSb
Formula weight	1462.28
Temperature/K	138(3)
Crystal system	trigonal
Space group	R3
a/Å	14.0505(5)
b/Å	14.0505(5)
c/Å	21.0782(8)
α/°	90
β/°	90
γ/°	120
Volume/Å ³	3603.7(3)
Z	3
ρ _{calc} /cm ³	2.021
μ/mm ⁻¹	7.426
F(000)	2106.0
Crystal size/mm ³	0.2 × 0.2 × 0.15
Radiation	Mo Kα (λ = 0.71073)
2θ range for data collection/°	3.864 to 65.416
Index ranges	-21 ≤ h ≤ 21, -21 ≤ k ≤ 21, -28 ≤ l ≤ 31
Reflections collected	15370
Independent reflections	5316 [R _{int} = 0.0212, R _{sigma} = 0.0237]
Data/restraints/parameters	5316/1/155
Goodness-of-fit on F ²	1.062
Final R indexes [I ≥ 2σ (I)]	R ₁ = 0.0257, wR ₂ = 0.0596
Final R indexes [all data]	R ₁ = 0.0324, wR ₂ = 0.0618
Largest diff. peak/hole / e Å ⁻³	0.93/-0.55
Flack parameter	0.390(10)

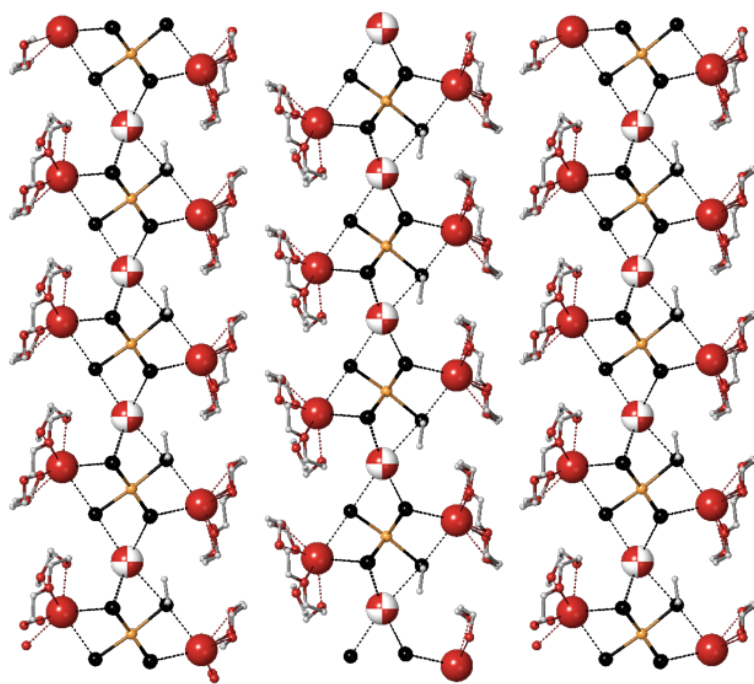


Figure S1. Packing in $[\text{C}@\text{Cs}]_2\text{CsSbBr}_6$ showing how Cs (not coordinated to crown ether, open circles) coordinates SbBr_6 units and creates 1D extended structure.

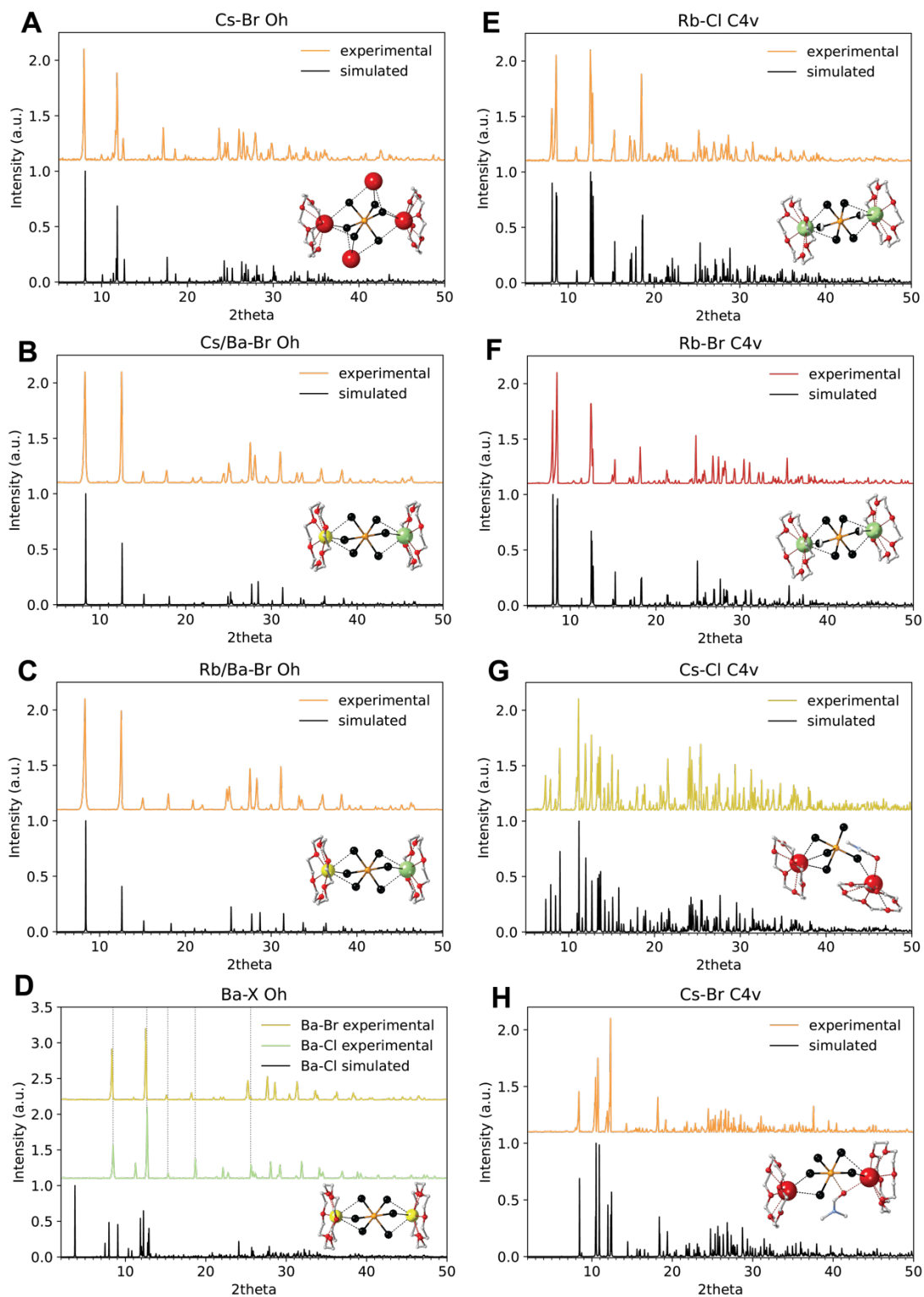


Figure S2. Experimental and simulated PXRD patterns of (A) $[C@Cs]_2CsSbBr_6$, (B) $[C@Cs][C@Ba][SbBr_6]$, (C) $[C@Rb][C@Ba][SbBr_6]$, (D) $[C@Ba]_4[SbBr_6]_2[Sb_2Br_8]$ and $[C@Ba]_4[SbCl_6]_2[Sb_2Cl_8]$, (E) $[C@Rb]_2SbCl_5$, (F) $[C@Rb]_2SbBr_5$, (G) $[C@Cs]_2SbCl_5$, (H)

$C@Cs_2SbBr_5$. In case of $[C@Ba]_4[SbBr_6]_2[Sb_2Br_8]$ and $[C@Ba]_4[SbCl_6]_2[Sb_2Cl_8]$, the difference between simulated and experimental data might come from the fact that during slow growth of single crystal, DMF molecules are co-crystallized, while in the powder form, DMF molecules might partially leave and lead to a collapse of structure into more symmetric one.

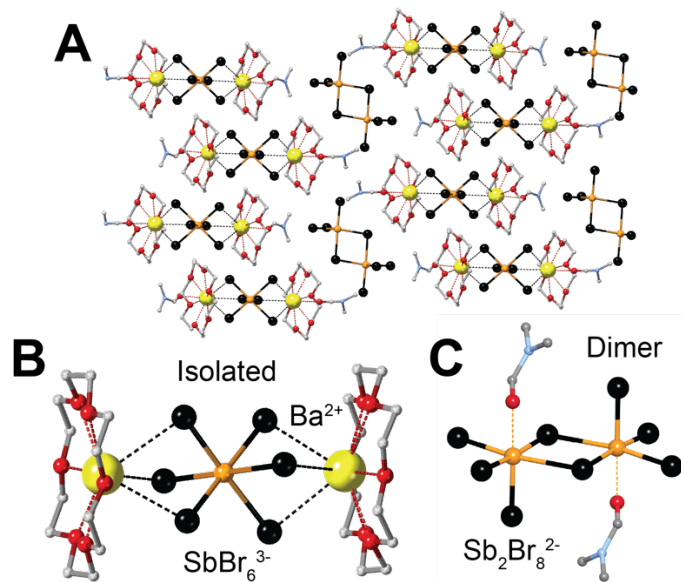


Figure S3. (A) Packing of the $[C@Ba]_4[SbBr_6]_2[Sb_2Br_8]$. (B) Isolated octahedral units. (C) Isolated square pyramidal dimer units with each DMF molecule having 50% of occupancy.

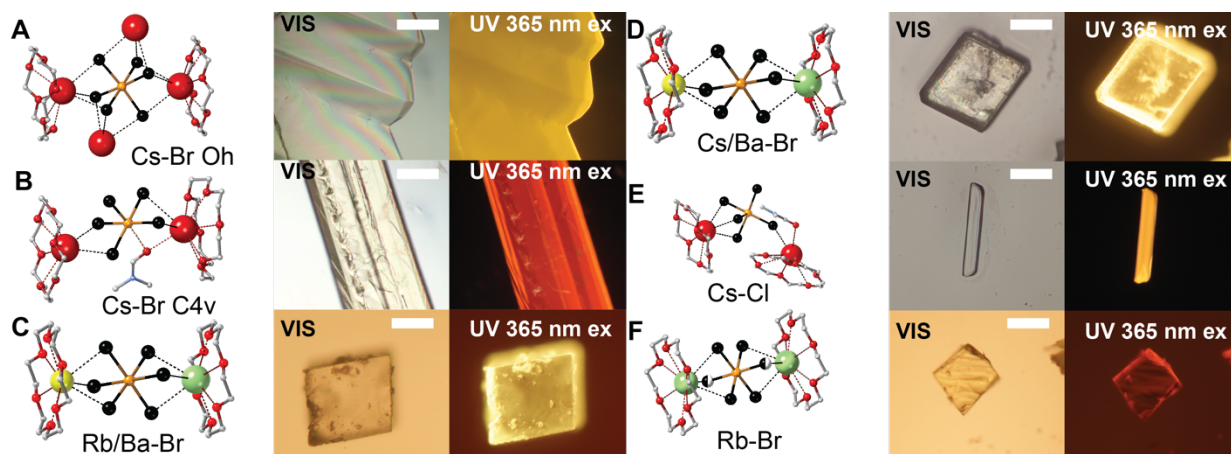


Figure S4. Optical microscope images of crystalline samples under ambient and UV light (365 nm) of (A) $[C@Cs]_2CsSbBr_6$, (B) $[C@Cs]_2SbBr_5$, (C) $[C@Rb][C@Ba][SbBr_6]$, (D) $[C@Cs][C@Ba][SbBr_6]$, (E) $[C@Cs]_2SbCl_5$, (F) $[C@Rb]_2SbBr_5$. The scalebar is 1 mm.

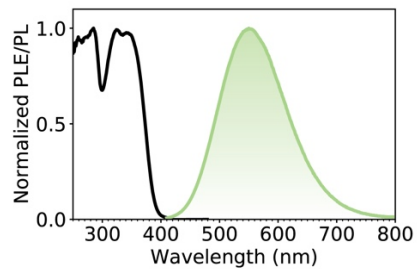


Figure S5. PL and PLE of the $[C@Ba]_4[SbCl_6]_2[Sb_2Cl_8]$.

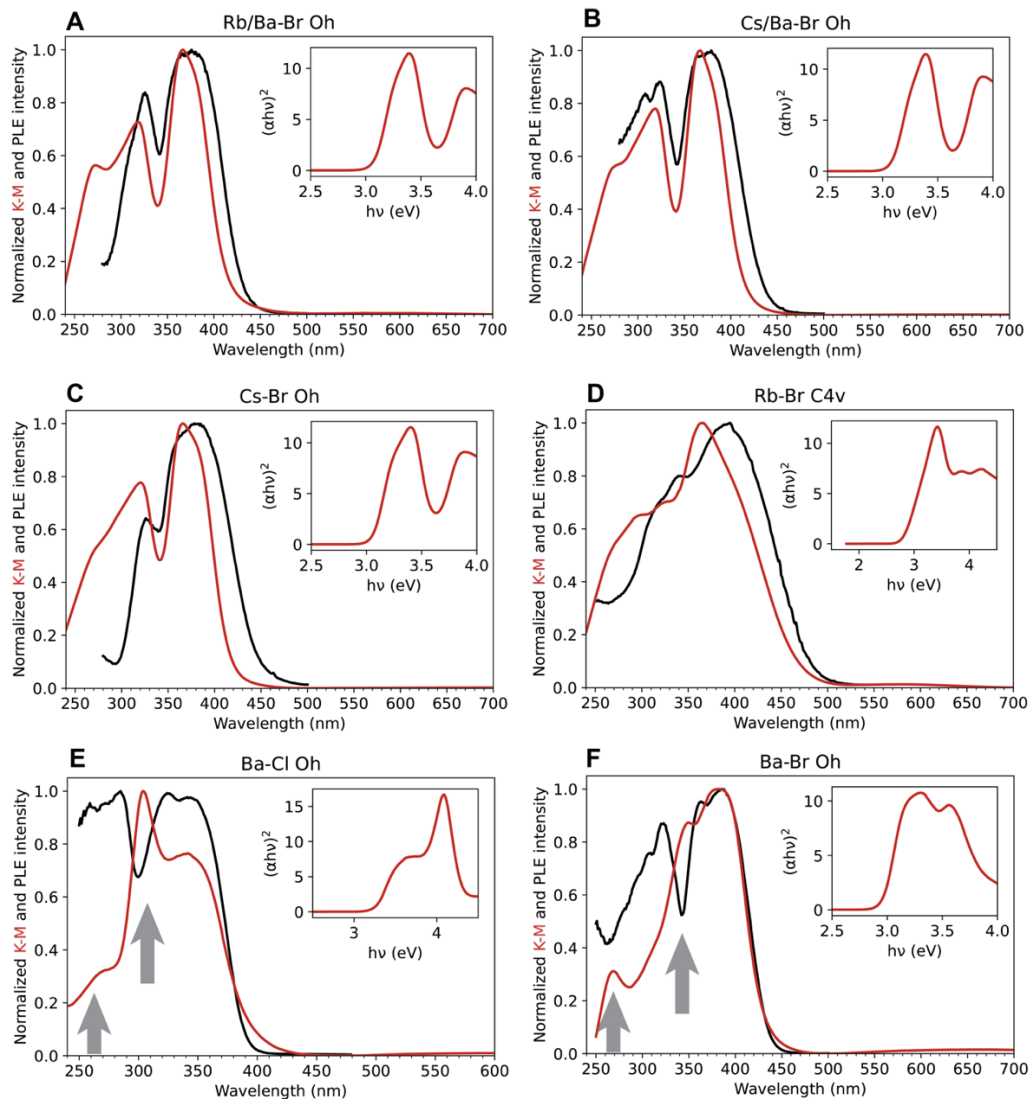


Figure S6. Comparison of PLE and Kubelka-Munk spectra for (A) $[C@Rb][C@Ba][SbBr_6]$, (B) $[C@Cs][C@Ba][SbBr_6]$, (C) $[C@Cs]_2CsSbBr_6$, (D) $[C@Rb]_2SbBr_5$, (E) $[C@Ba]_4[SbCl_6]_2[Sb_2Cl_8]$, (F) $[C@Ba]_4[SbBr_6]_2[Sb_2Br_8]$. The black arrows are indicating positions where $Sb_2X_8^{2-}$ fragments are absorbing but do not appear in the PLE spectra. Tauc plot (inset) evidences of a direct allowed transition.

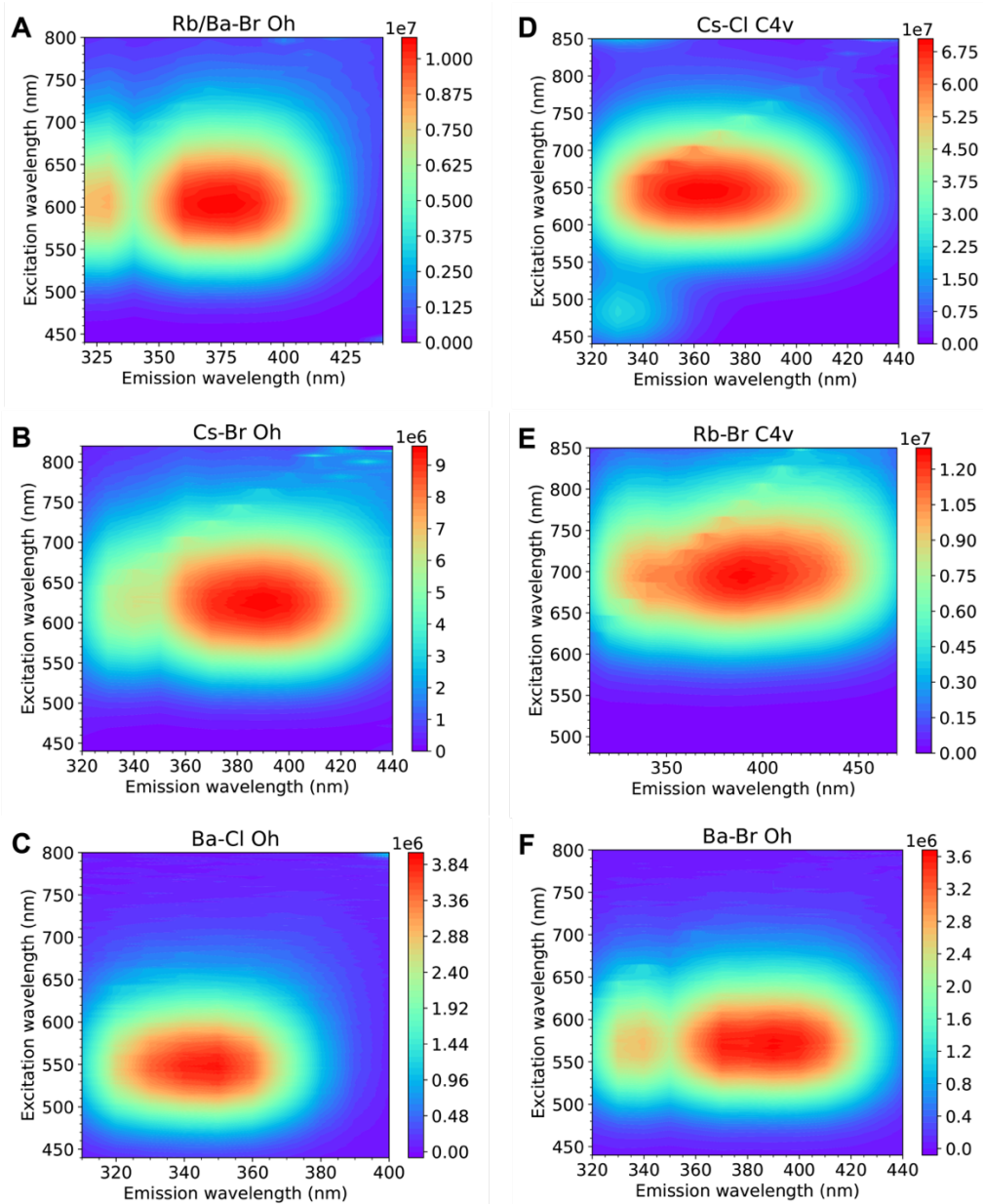


Figure S7. A 2D PL/PLE maps of A) $[C@Rb][C@Ba][SbBr_6]$, (B) $[C@Cs]_2CsSbBr_6$, (C) $[C@Ba]_4[SbCl_6]_2[Sb_2Cl_8]$, (D) $[C@Cs]_2SbCl_5$, (E) $[C@Rb]_2SbBr_5$, (F) $[C@Ba]_4[SbBr_6]_2[Sb_2Br_8]$.

Table S10. Optical properties (PL peak position, fwhm, PLE peak, Stokes shift, PLQY) for the obtained antimony(III) halide hybrids

Compound	PL peak position, nm (eV)	fwhm, meV (nm)	PLE peak, nm (eV)	Stokes shift, eV (nm)	PLQY, %
[C@Rb] ₂ SbCl ₅	686 (1.81)	428 (165)	340 (3.65)	1.84 (346)	75 ¹
[C@Rb] ₂ SbBr ₅	713 (1.74)	381 (158)	395 (3.14)	1.39 (318)	56 ³
[C@Cs] ₂ SbCl ₅	664 (1.87)	413 (149)	344 (3.61)	1.77 (320)	89 ¹
[C@Cs] ₂ SbBr ₅	682 (1.82)	349 (132)	395 (3.14)	1.32 (287)	27 ³
[C@Ba] ₄ [SbCl ₆] ₂ [Sb ₂ Cl ₈]	569 (2.18)	505 (143)	341 (3.64)	1.46 (228)	57 ²
[C@Ba] ₄ [SbBr ₆] ₂ [Sb ₂ Br ₈]	591 (2.10)	481 (137)	385 (3.22)	1.12 (206)	46 ²
[C@Rb][C@Ba][SbBr ₆]	617 (2.01)	498 (155)	376 (3.30)	1.29 (241)	40 ²
[C@Cs][C@Ba][SbBr ₆]	643 (1.93)	509 (173)	379 (3.27)	1.34 (264)	45 ²
[C@Cs] ₂ CsSbBr ₆	657 (1.89)	462 (163)	375 (3.31)	1.41 (282)	11 ²

PLQY measured with 360 nm excitation,¹ 390 nm excitation,² 400 nm excitation.³

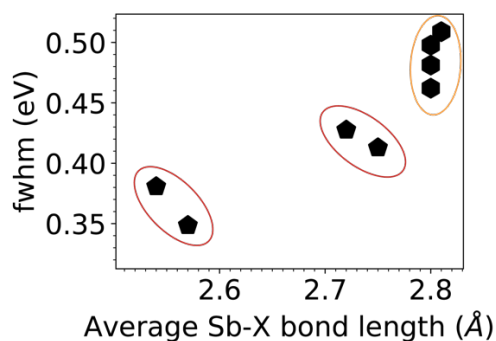


Figure S8. PL fwhm dependence on the average Sb-X bond.

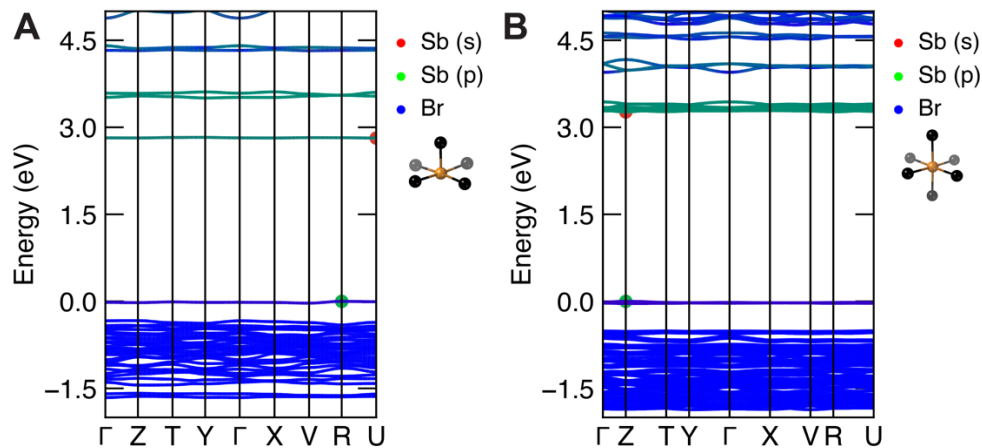


Figure S9. Orbital-projected band structure plots for (A) $[C@Rb]_2SbBr_5$ and (B) $[C@Cs][C@Ba]SbBr_6$. The valence band maximum and conduction band minimum are denoted with green and red dots, respectively. $[C@Rb]_2SbBr_5$ features an indirect band gap of 2.814 eV, while $[C@Cs][C@Ba]SbBr_6$ has a direct band gap of 3.265 eV.

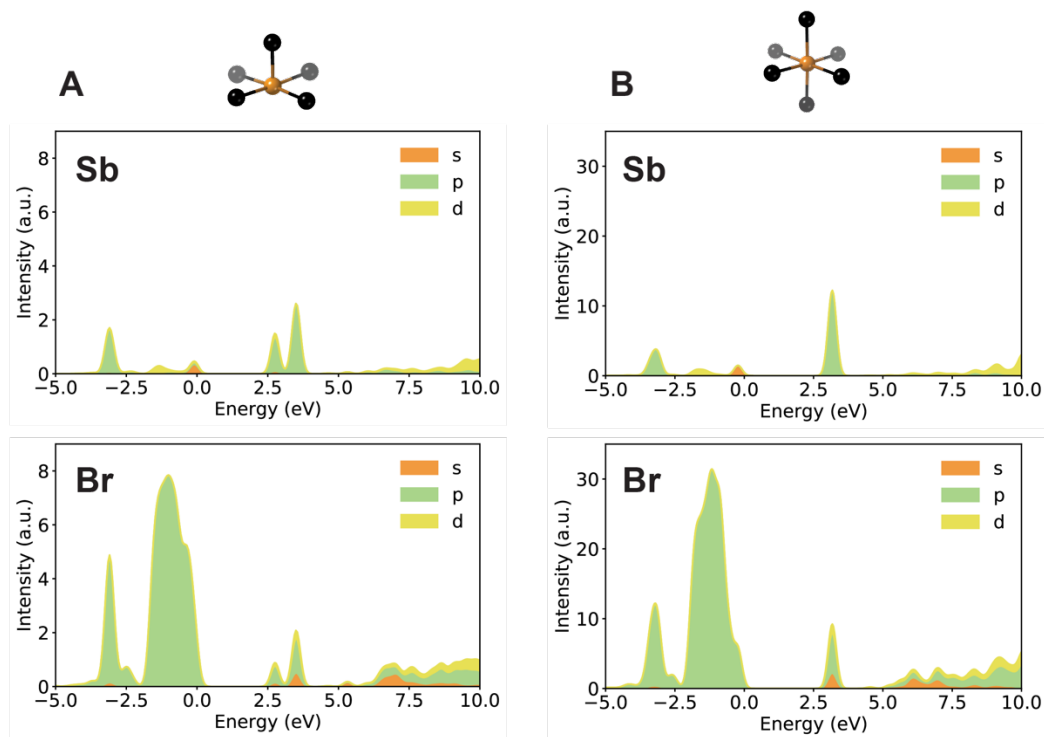


Figure S10. Orbital-decomposed cumulative DOS of (A) $[C@Rb]_2SbBr_5$ and (B) $[C@Cs][C@Ba][SbBr_6]$ (bottom); other atomic contributions (O, C, H, *etc.*) are omitted for clarity.

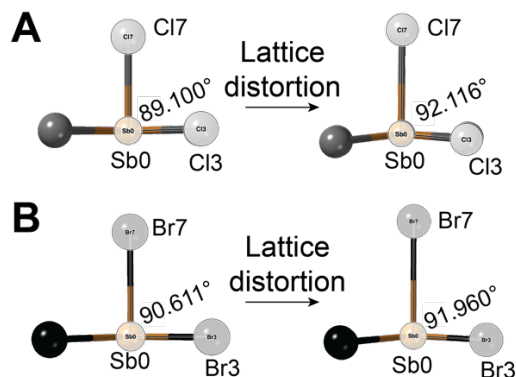


Figure S11. (A) Structural change from ground to the excited state in $[\text{C}@\text{Rb}]_2\text{SbCl}_5$, depicting specifically the change in the angle between an axial Chlorine atom (Cl7) and equatorial Chlorine atoms (e.g., Cl3) from 89.1 to 92.12. (B) Structural change from ground to the excited state in $[\text{C}@\text{Rb}]_2\text{SbBr}_5$, depicting specifically the change in the angle between an axial Bromine atom (Br7) and equatorial Bromine atoms (e.g., Br3) from 90.61 to 91.96. The higher change in case of Chlorine can be responsible for a larger Stokes shift in square pyramidal antimony(III) chlorides. This is related to the higher stereoactivity of the lone pair (oriented on the other side of the axial halide atom X7) in case of chlorides, which results in stronger repulsion between the lone pair and equatorial Chlorine atoms (the angle $89.1 < 90$).

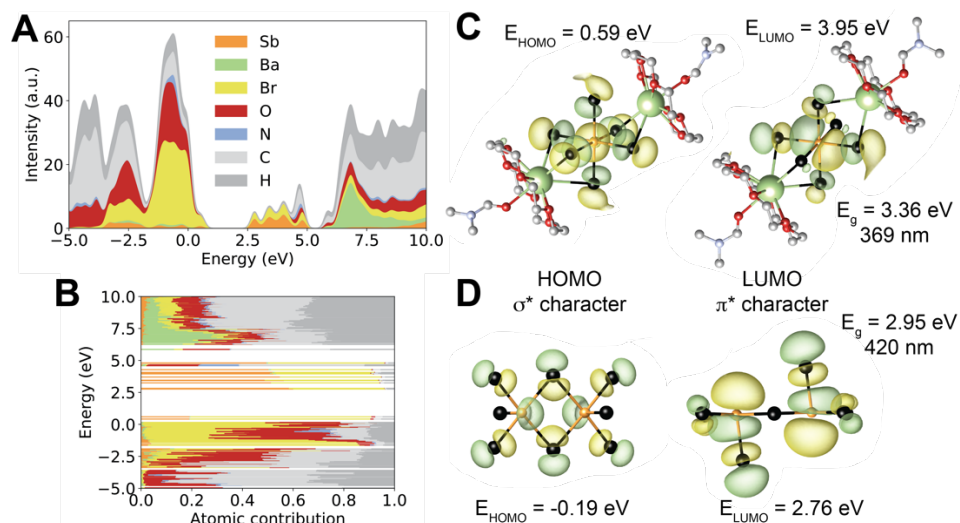


Figure S12. (A) DOS of $[\text{C}@\text{Ba}]_4[\text{SbBr}_6]_2[\text{Sb}_2\text{Br}_8]$. (B) Electronic structure of $[\text{C}@\text{Ba}]_4[\text{SbBr}_6]_2[\text{Sb}_2\text{Br}_8]$ with atomic contributions normalized from 0 to 1, the contribution of each atom type to a given MO is represented with a different color. (C) Atomically projected MO of an isolated octahedral unit in $[\text{C}@\text{Ba}]_4[\text{SbBr}_6]_2[\text{Sb}_2\text{Br}_8]$; the energy gap between HOMO and LUMO of the octahedral unit is 3.95 eV. (D) Atomically projected MO of an isolated square pyramidal dimer unit in $[\text{C}@\text{Ba}]_4[\text{SbBr}_6]_2[\text{Sb}_2\text{Br}_8]$; the energy gap between HOMO and LUMO of the octahedral unit is 2.95 eV.

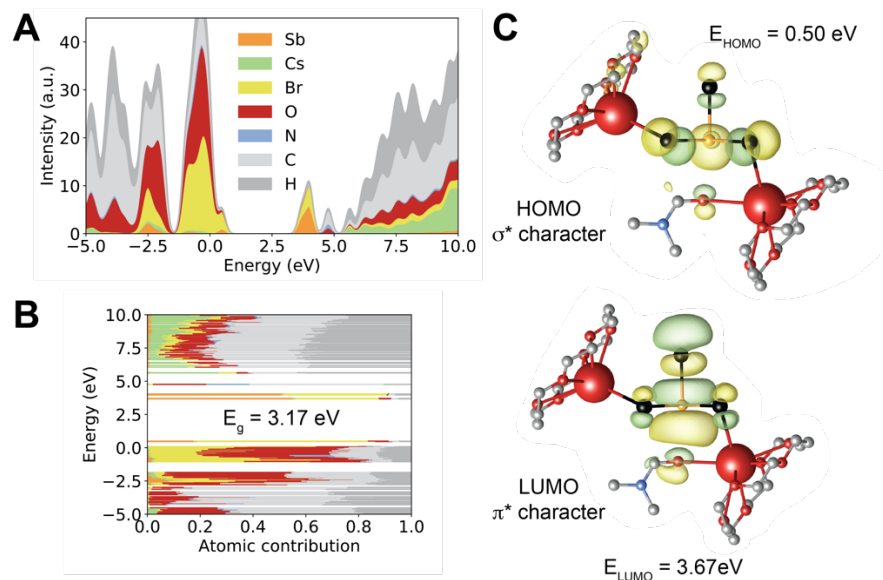


Figure S13. (A) DOS of $[\text{C}@\text{Cs}]_2\text{SbBr}_5$. (B) Electronic structure of $[\text{C}@\text{Cs}]_2\text{SbBr}_5$ with atomic contributions normalized from 0 to 1, the contribution of each atom type to a given MO is represented with a different color. (C) Atomically projected MO of an isolated square pyramidal unit in $[\text{C}@\text{Cs}]_2\text{SbBr}_5$. Both in HOMO and LUMO, Oxygen p -orbitals are contributing to the electronic states. The energy gap between HOMO and LUMO is 3.17 eV.

Table S11. The results of mono or biexponential fitting of the RT decay times for a range of crown-ether 0D Sb compounds: τ_1 and τ_2 are shorter and longer decay constants, respectively.

Compound	τ_1 , ns	τ_2 , ns
$[\text{C}@\text{Rb}]_2\text{SbCl}_5$	608	4857
$[\text{C}@\text{Rb}]_2\text{SbBr}_5$		2286.3
$[\text{C}@\text{Cs}]_2\text{SbCl}_5$		5261.9
$[\text{C}@\text{Cs}]_2\text{SbBr}_5$		827.7
$[\text{C}@\text{Ba}]_4[\text{SbCl}_6]_2[\text{Sb}_2\text{Cl}_8]$		2828.4
$[\text{C}@\text{Ba}]_4[\text{SbBr}_6]_2[\text{Sb}_2\text{Br}_8]$	366	1397.2
$[\text{C}@\text{Rb}][\text{C}@\text{Ba}][\text{SbBr}_6]$	452	1663
$[\text{C}@\text{Cs}][\text{C}@\text{Ba}][\text{SbBr}_6]$		1276
$[\text{C}@\text{Cs}]_2\text{CsSbBr}_6$	207.6	1061.3

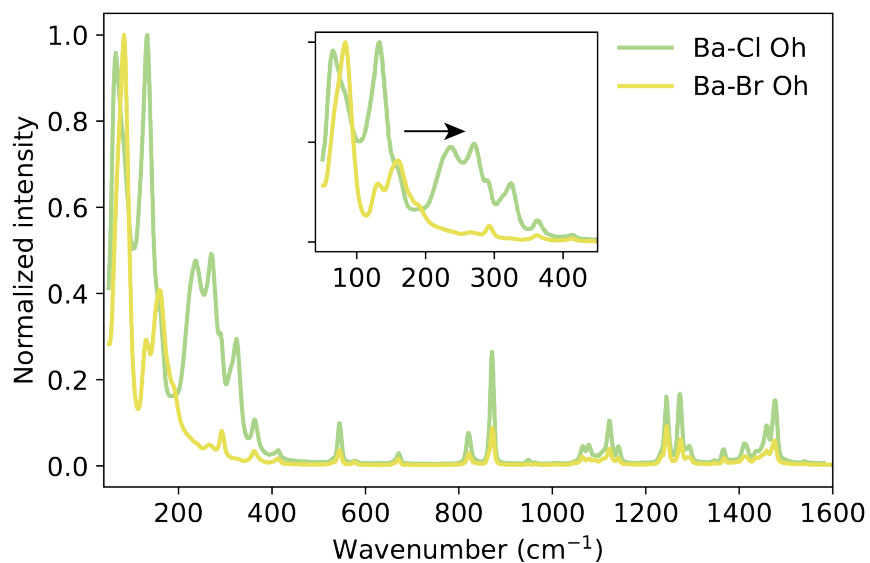


Figure S14. Raman spectra of $[\text{C@Ba}]_4[\text{SbCl}_6]_2[\text{Sb}_2\text{Cl}_8]$ and $[\text{C@Ba}]_4[\text{SbBr}_6]_2[\text{Sb}_2\text{Br}_8]$. The black arrow is demonstrating how the vibration frequency is increased from Sb-Br to Sb-Cl bond.

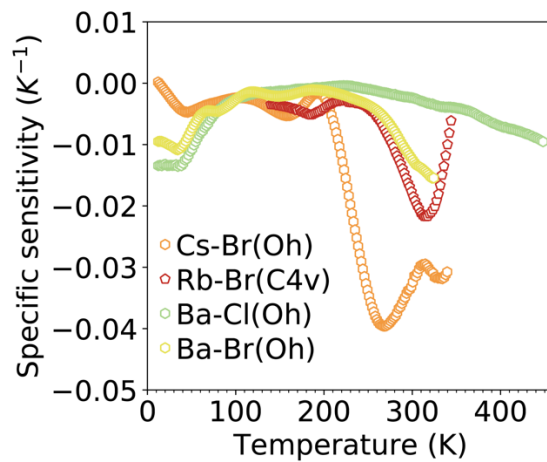


Figure S15. Specific sensitivity, $\alpha = -\frac{d\tau}{dT} \cdot \frac{1}{\tau}$, for a range of crown-ether based compounds.

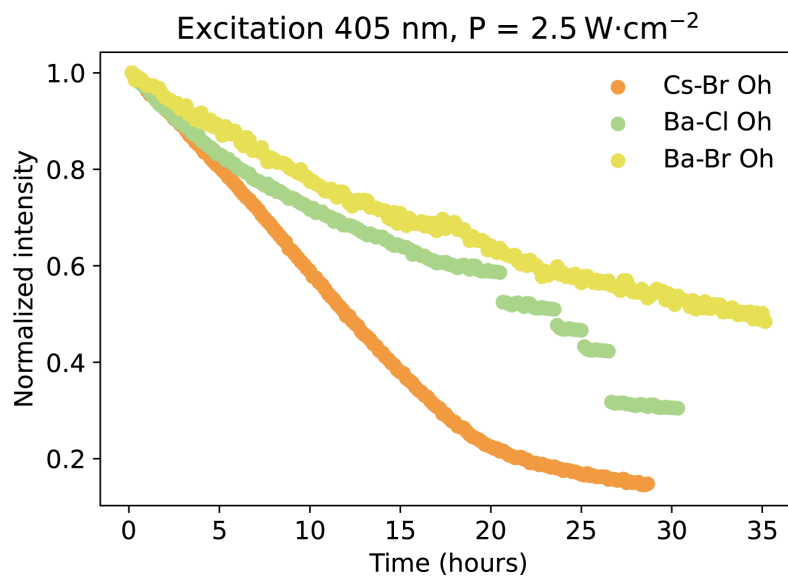


Figure S16. Photostability test for [C@Cs]₂CsSbBr₆, [C@Ba]₄[SbCl₆]₂[Sb₂Cl₈] and [C@Ba]₄[SbBr₆]₂[Sb₂Br₈].

References

1. Sheldrick, G. M., Crystal Structure Refinement with SHELXL. *Acta Cryst. C* **2015**, *71*, 3-8.
2. Dolomanov, O. V.; Bourhis, L. J.; Gildea, R. J.; Howard, J. A. K.; Puschmann, H., OLEX2: a Complete Structure Solution, Refinement and Analysis Program. *J. Appl. Crystallogr.* **2009**, *42*, 339-341.